Research Article | Vol. 29, No. 11 / 24 May 2021 / Optics Express 16469

Optics EXPRESS

Field-based design of a resonant dielectric antenna for coherent spin-photon interfaces

LINSEN LI,[1] HYEONGRAK CHOI,[1] MIKKEL HEUCK,[1,2] AND DIRK ENGLUND[1,3]

[1] *Research Laboratory of Electronics, Massachusetts Institute of Technology, Cambridge, MA 02139, USA*
[2] *mheuck@mit.edu*
[3] *englund@mit.edu*

Abstract: We propose a field-based design for dielectric antennas to interface diamond color centers in dielectric membranes with a Gaussian propagating far field. This antenna design enables an efficient spin-photon interface with a Purcell factor exceeding 400 and a 93% mode overlap to a 0.4 numerical aperture far-field Gaussian mode. The antenna design with the back reflector is robust to fabrication imperfections, such as variations in the dimensions of the dielectric perturbations and the emitter dipole location. The field-based dielectric antenna design provides an efficient free-space interface for closely packed arrays of quantum memories for multiplexed quantum repeaters, arrayed quantum sensors, and modular quantum computers.

1. Introduction

A central goal in quantum optics is the development of efficient interfaces between a given free-space propagating optical field and a quantum emitter dipole. In solid-state materials, color centers in diamond are among the leading systems [1–6], but high-cooperativity interfaces remain an open challenge [7]. Quantum applications such as quantum network [8], computing [9], and sensing [10], demand an efficient coupling of quantum emitters to free-space propagating fields. To improve photonic interfaces to free-space modes, recent works developed a range of structures including parabolic reflectors [11], macroscopic solid immersion lenses [12,13], circular gratings [14–16], metal plasmonic gratings [17,18], metallic bow-tie antennas [19], nanopatch antennas [20], dielectric metasurface [21], metasurface lenses [22], and diamond nanopillars [23]. However, none of these designs combines a high Purcell effect and directional emission to jointly optimize spectral and spatial collection.

Here, we introduce a new approach: starting from the radiation field of a dipole emitter in a 2D dielectric slab (of approximately half-wavelength thickness), we create perturbations to transform to the desired output and optimize power transfer through the cavity Purcell effect. This 'field-based design' also introduces a novel 3D transfer-matrix approach that extends the widely used 1D transfer matrix method used in dielectric mirror design, etc.

We start from a dipole in a diamond membrane and apply this field-based design recipe to develop a dielectric antenna with a back reflector to match atomic dipole emission to a targeted free-space propagating mode. We consider, in particular, the emission from a nitrogen-vacancy (NV) center with zero-phonon emission at $\lambda \sim 637$ nm located in a 150 nm ($\approx \lambda/2n$) thick slab, where $n = 2.4$ is the refractive index of diamond. This diamond antenna simultaneously achieves a Purcell factor of 420 and a 93% mode overlap with 0.4 numerical aperture (NA) Gaussian beam, which has a 99% collection efficiency within an NA of 0.5. Thus, we estimate that the spin-photon interface efficiency can improve $\gtrsim 300$ times compared with an NV dipole embedded in a 150 nm thick diamond membrane without nanostructures. Dielectric antennas, unlike metallic antennas [19], do not suffer from Ohmic loss and quenching. The surface charge and spin noise are also alleviated by placing the closest etched surface more than one wavelength

#419773
Journal © 2021

https://doi.org/10.1364/OE.419773
Received 11 Feb 2021; revised 14 Apr 2021; accepted 19 Apr 2021; published 13 May 2021

away from the dipole emitter [24]. We believe this antenna structure to be of great utility for quantum applications with quantum emitters.

2. Antenna design

As a figure of merit, we consider a coherent spin-photon interface efficiency $\eta = \eta_1\eta_2$, where η_1 denotes the spin-antenna interface efficiency and η_2 is the antenna efficiency. The spin-antenna interface efficiency η_1 is defined as

$$\eta_1 = \frac{\eta_0 \times F_p}{\eta_0 \times F_p + 1 - \eta_0}, \tag{1}$$

where η_0 denotes the radiation efficiency into the zero-phonon line (ZPL). Here, the values of η_0 for nitrogen-vacancy, silicon-vacancy, and tin-vacancy centers are 3%, 7%, and 32%, respectively [6]. F_p is the Purcell Factor, which increases the spontaneous emission rate of the ZPL [25].

The antenna far field $\vec{E}_{\text{far}} = E_r\vec{r} + E_\theta\vec{\theta} + E_\phi\vec{\phi}$ is calculated on a hemispherical surface located r_0 = 1 m away from the center dipole source with finite-difference time-domain (FDTD) simulations using Lumerical. We expect that E_r to be zero because the electric far field is perpendicular to the direction of propagation. Assuming a monochromatic antenna far field with angular frequency ω and corresponding free-space wavelength λ, $\vec{E}_{\text{far}}(r_0, \theta, \phi, t) = C_{\text{far}} \exp[-i(\omega t - \frac{2\pi r_0}{\lambda})]\vec{e}_{\text{far}}(\theta, \phi)$, where C_{far} is the far-field amplitude. $\vec{e}_{\text{far}}(\theta, \phi)$ is the dimensionless normalized vector. $\vec{e}_{\text{far}}(\theta, \phi)$ satisfies $\int_0^{2\pi}\int_0^{\pi} |\vec{e}_{\text{far}}(\theta, \phi)|^2 \sin\theta \mathrm{d}\theta\mathrm{d}\phi = T_z = P_z/(2P_x + 2P_y + P_z)$, where T_z is the fraction of the emitted power propagating in the $+z$ direction. P_x, P_y, and P_z are the radiated power propagating in the x, y, and z direction, respectively (Fig. 1(a)). The target far field $\vec{E}_{\text{tar}}(r_0, \theta, \phi, t)$ has the same notation except the subscript.

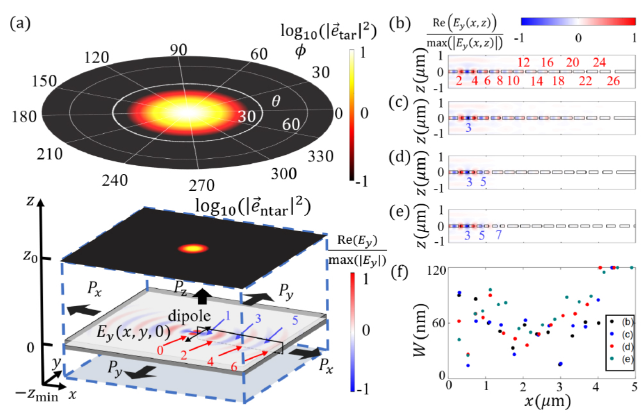

Fig. 1. Illustration of the field-based antenna design recipe. (a) 2D plots of the target far field $\log_{10}(|\vec{e}_{\text{tar}}|^2)$ (top), the target near field $\log_{10}(|\vec{e}_{\text{ntar}}|^2)$ (middle), and illustration of the unpatterned diamond slab overlaid with the dipole field $\text{Re}(E_y)/\max(|E_y|)$ labeled with phase front number, assuming a perfect reflector at the $z = -z_{\text{min}}$ plane in the final structure. (b-e) Cross-sections of the diamond slab in the x-z plane [black rectangle plane in (a)] with the electric field $\text{Re}(E_y(x,z))/\max(|E_y(x,z)|)$ overlaid. Slots are located at the even phase fronts (2, 4,. . . , 26) in (b) for constructive interference. We add extra destructive interference slots around odd phase fronts in (c) (3), (d) (3 and 5), and (e) (3, 5, and 7). The black line shows the slot edges. (f) Slot locations and widths for the antenna designs in (b-e).

Optics EXPRESS

The antenna efficiency η_2 is the square of the mode overlap between the antenna far field $\vec{e}_{\text{far}}(\theta,\phi)$ and target far field $\vec{e}_{\text{tar}}(\theta,\phi)$, which we define as

$$\eta_2 = \left| \int_0^{2\pi} \int_0^{\pi} \vec{e}_{\text{far}}(\theta,\phi) \cdot \vec{e}^{\,*}_{\text{tar}}(\theta,\phi) \sin\theta \mathrm{d}\theta \mathrm{d}\phi \right|^2 . \tag{2}$$

We use a polarized Gaussian beam with NA = 0.4 as the target far field, $\vec{e}_{\text{tar}}(\theta,\phi) = 2.10 \times \exp(-\tan^2\theta/0.4^2)\vec{y}$, which has 99% of its electromagnetic energy within an NA of 0.5. Here, $\vec{e}_{\text{tar}}(\theta,\phi)$ satisfies $\int_0^{2\pi} \int_0^{\pi} |\vec{e}_{\text{tar}}(\theta,\phi)|^2 \sin\theta \mathrm{d}\theta \mathrm{d}\phi = 1$. We also consider the higher order correction for the polarized Gaussian beam [26], $\vec{e}_{\text{tar}}(\theta,\phi) = 2.14 \times \exp(-\tan^2\theta/0.4^2)[(1-\tan^2\theta\sin^2\phi)\vec{y} - \tan^2\theta\sin\phi\cos\phi\vec{x} - \tan\theta\sin\phi(1-\tan^2\theta/2)\vec{z}]$. It has less than 1% variation in our final efficiency calculation. Our design applies the mode overlap between the antenna far field and the target Gaussian far field as a part of the figure of merit. This estimates the single-mode fiber collection efficiency, which is important in quantum photonic applications.

We summarize the field-based antenna design recipe as follows, with the details of each step in the supplementary material:

Step 1: calculate the field profile of y-oriented dipole, $\text{Re}[E_y(x,y,0)]/\max(|E_y(x,y,0)|)$, in the 150 nm thick unpatterned diamond membrane, as shown in Fig. 1(a). Here the 150 nm (approximate half-wavelength thickness) is chosen for ensuring the single slab mode at 637 nm. We can choose a different starting thickness for different target wavelengths. We define the n^{th} phase front as the points with $n\pi$ phase difference from the dipole. The red arrows in Fig. 1(a) indicate the even number phase fronts, which will provide constructive interference when added to the membrane. While the blue arrows indicate the odd number phase fronts, of which scattering will make destructive interference with the scattering from the even number phase fronts. We transform the target far field $\vec{e}_{\text{tar}}$ to the target near field $\vec{e}_{\text{ntar}}$, which has azimuthal symmetry in amplitude. We add dielectric perturbations along the phase fronts to make the slab mode normally incident on each perturbation layer. Each curved perturbation layer is then approximated by a curved slot or periodic array of holes. In this construction, we approximated the 3D problem with a 2D problem for the slots (x-z plane) or with a periodic boundary condition in the y direction for the hole array.

Step 2: simulate the in-plane transverse-electric (TE) slab mode that is normally incident on a single slot (width w) or a single period of the hole array (diameter d, spacing L) with FDTD simulation. The simulation yields a lookup table with reflection and transmission coefficients as well as scattered near field distributions $\vec{E}_s(x) = \vec{E}_{\text{near}}(x,z_0)$ for slots or $\vec{E}_s(x) = \frac{1}{L}\int_0^L \vec{E}_{\text{near}}(x,y,z_0)\mathrm{d}y$ for hole spacing L. The i^{th} layer is at position x_i with slot width w_i or hole parameters (d_i, L_i). Here, $i = 1,\ldots,N_{\max}$, where $N_{\max}$ is the maximum number of the perturbation layers in the antenna.

Step 3: apply transfer matrix model (TMM) to calculate the electric field at each layer [27,28]. Thus, we obtain the total scattered near field by coherently adding contributions from each scattering layer using the lookup table. Here we use the slots located at even $(2,4,6,\ldots,26)$ phase fronts of the dipole field in the unpatterned diamond slab as an initial guess.

Step 4: calculate the mode overlap between the target and the antenna-scattered near field along the line $(x, y=0, z=z_0)$. The parameters (x_i, w_i) or (x_i, d_i, L_i) of each layer are optimized based on step 3 to maximize the mode overlap.

Step 5: curve each slot or layer of holes to match the dipole emission phase fronts in the diamond membrane (centered at $z=0$) and add a bottom reflector at $z=-z_{\min}$. We apply a gradient descent optimization to maximize η calculated from 3D FDTD simulations using the result from step 4 as an initial guess.

Step 6: add destructive interference slots (located at odd dipole field phase fronts like 3, 5, and 7) in the initial guess structure in step 3 and redo step 4 and step 5 to increase the antenna Purcell factor.

Optics EXPRESS

Figure 1(b-e) plot the optimized antenna x-z cross-sections of step 4 overlaid with the electric field $\mathrm{Re}(E_y(x,z))/\max(|E_y(x,z)|)$ without, with one, with two, and with three destructive interference slots in the initial guess structure, respectively. Figure 1(f) details the values for slot locations and widths in Fig. 1(b-e). We optimized the value of the slot widths using the transfer matrix model, as described in the supplemental material. As seen in Fig. 1(f), the optimized slot widths first decrease and then increase as a function of the distance to the dipole x. This trend causes scattering that most closely resembles the Gaussian-like near field that is the field distribution in the Fourier plane of the desired Gaussian-cross-section far-field distribution.

3. Simulation results

Figure 2(a) plots the efficiency as a function of the number of the destructive interference slots. η increases with the number of destructive interference slots but saturates after four slots since the field is confined in the central region as shown in Fig. 2(b). Figure 2(b) shows the slot antenna design with an efficiency η = 75% for NVs using four destructive interference slots located at phase fronts (3, 5, 7, and 9) (See supplementary material for detailed geometries). Figure 2(c) plots the spectrum of the Purcell factor and far-field distribution of the antenna emission.

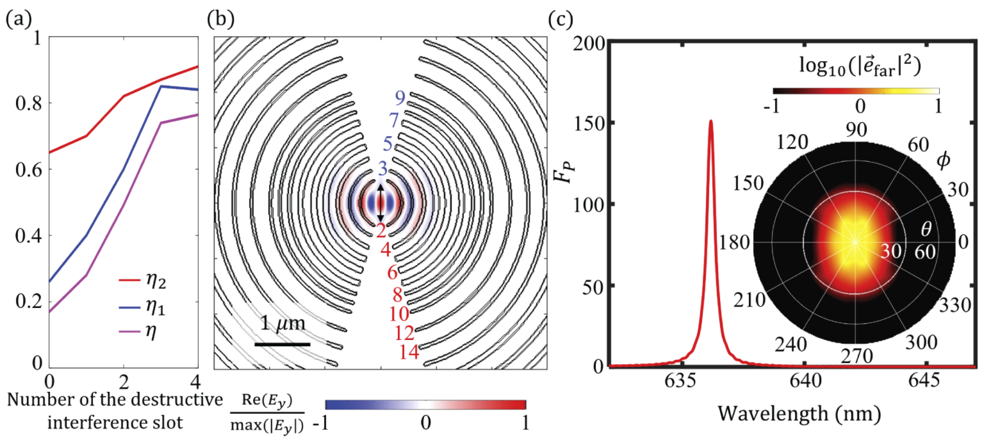

Fig. 2. (a) Efficiency vs. number of the destructive interference slots. (b) $\mathrm{Re}(E_y)/\max(|E_y|)$ of the antenna with four destructive interference slots (at phase fronts 3, 5, 7, and 9). The black line shows the edge of the slot in the antenna structure. The red texts label phase front number of the constructive interference slots while the blue texts label the destructive interference slots. (c) Purcell factor spectrum and the far-field distribution $\log_{10}(|\vec{e}_{far}|^2)$ of the antenna structure in (b).

Next, we use arrays of holes as the perturbation layer. The holes in the design have a minimum diameter (70 nm), which is larger than the minimum width of the slot (40 nm) relaxing fabrication difficulties. In addition, the design with holes ensures a connected suspended structure even if the holes wrap around 360° with more degrees of freedom by hole radii and spacing.

Figure 3(a) shows the holey dielectric antenna structure along with the emitted far field. Figure 3(b) plots the spectrum of the Purcell factor and electric field distribution in the antenna's x-y cross-section. For the NV center in an unpatterned 150 nm thick diamond membrane, η_1 is only 3% and η_2 is only 9%, which gives a total η of 0.27%. After adding the holes with optimized positions and sizes, the resulting η of the antenna structure in Fig. 3 reaches 81% with a large Purcell factor of 420 with corresponding Q ≈ 4400 (η_1 = 93%) and a large mode overlap (η_2 = 87%) simultaneously. We optimized the structure for NV centers in diamond here. The design process can also work for other emitters by changing the target resonant wavelength. In the supplementary material, we also show an antenna design for the GaAs quantum dot system. In Fig. 3(a), the distance between the emitter and the closest dielectric perturbation is larger than λ/n_d (the resonant wavelength in the material, where n_d is the refractive index of the diamond), which can alleviate surface-charge noise. A previously reported bullseye antenna design has a collection efficiency of 90% within NA = 0.65 and a Purcell factor of 20 in a GaAs quantum dot system [14]. Our design applies the mode overlap between the antenna far field and the target Gaussian far field as the figure of merit to have a better estimation in single-mode fiber collection efficiency, which is important for quantum photonics, compared with the collection efficiency only considering the electromagnetic energy within a certain NA. Our design can simultaneously achieve a large mode overlap to a small NA mode and a large Purcell factor. The small NA collection can both provide lower magnification for a larger field of view to examine more quantum emitters and have a longer working distance between the objective lens and the cryogenic stage.

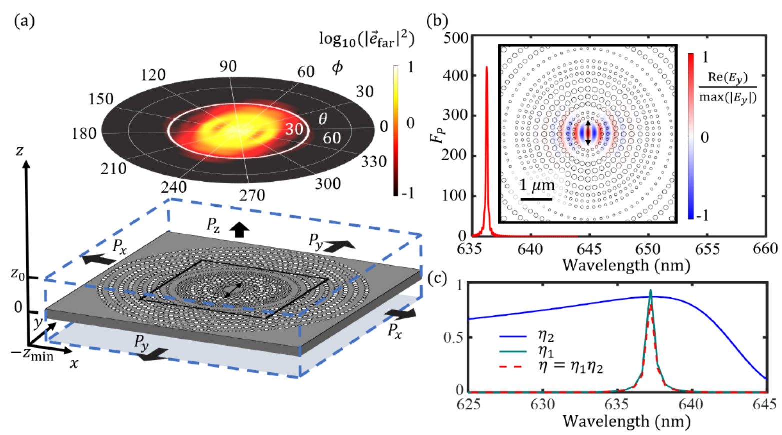

Fig. 3. (a) Illustration of the dielectric antenna structure, along with a plot of $\log_{10}(|\vec{e}_{\rm far}|^2)$ showing the far-field distribution. (b) Purcell factor spectrum of the antenna structure. The inset is a linear-scale plot of $\mathrm{Re}(E_y)/\max(|E_y|)$ corresponding to the black square region in (a). (c) The spin-photon interface efficiency η, spin-antenna interface efficiency η_1, and antenna efficiency η_2 as the function of wavelength for the antenna structure in (a).

4. Sensitivity analysis

The antenna design is tolerant to errors in dipole angle and location. Figure 4 plots the efficiencies and the Purcell factors as a function of the dipole's misalignment in location ($\Delta x, \Delta y, \Delta z$) and orientation, given by polar angle θ and azimuth angle ϕ. In Fig. 3, the simulated dipole orientation is in the y direction corresponding to $\theta = 0°$ and $\phi = 0°$. We define the normalized Purcell Factor $f_p = F_p/420$, where 420 is the maximum Purcell factor for the antenna structure in Fig. 3(b). Figure 4(a) and 4(b) show how η, η_2, and f_p vary with the dipole orientation.

Figure 4(c-e) summarize the effect of dipole displacements. The electric field changes rapidly in the x direction while changing gradually in the y direction, as seen in Fig. 3(b). Figure 4(c,d) show that the Purcell factor decreases by 80% for $\Delta x = 60$ nm, but only 20% for $\Delta y = 60$ nm. The Purcell factor drops 50% with $\Delta z = 60$ nm in Fig. 4(e). For our antenna design for NVs, the target implantation depth is 75 nm for the 150 nm diamond slab, which corresponds to a 60 keV implantation energy in Stopping and Range of Ions in Matter (SRIM) simulation [29]. From the simulation, we are 95% confident that the position variations of the implanted NV centers are within $|\Delta z|<32$ nm and $\sqrt{(\Delta x^2 + \Delta y^2)}<28$ nm under the Gaussian distribution assumption [29].

Optics EXPRESS

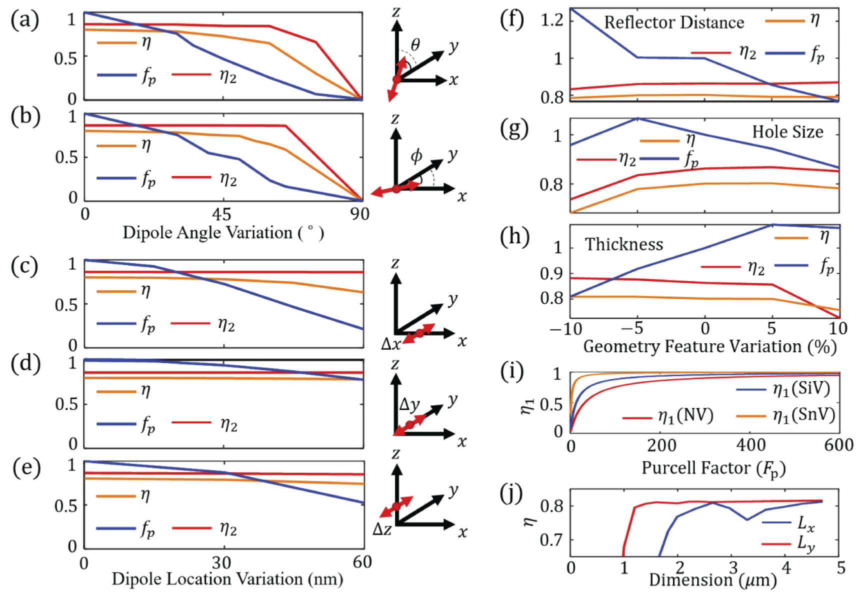

Fig. 4. The efficiencies η and η_2, as well as the normalized Purcell factor $f_p = F_p/420$ (420 is the maximum Purcell factor in Fig. 3(b)) as a function of changes in the dipole angle (θ, ϕ) (a, b), and dipole location $(\Delta x, \Delta y, \Delta z)$ (c-e), bottom reflector location (f), hole size (g), and membrane thickness (h), respectively. (i) Dependence of η_1 on the Purcell factors for different types of quantum emitters. (j) Efficiency η changes with L_x and L_y.

In summary, though the dipole location variation changes the Purcell factor, η_2 is changed less than 2% when the angle variation is smaller than 45° since the dipole couples to the antenna mode and the antenna mode couples to the free space target mode. f_p follows the expected overlap between the dipole $\vec{\mu}$ and the mode's electric field $\vec{E}$, i.e., $f_p \propto (\frac{|\vec{\mu}\cdot\vec{E}(r_i)|}{|\vec{\mu}|\cdot|\vec{E}_{max}|})^2$, where $\vec{E}(r_i)$ is the local electric field at the dipole emitter location r_i, and $|\vec{E}_{max}|$ is the maximum value of the electric field in the antenna [25].

We also investigate the variations of the bottom reflector distance, hole sizes, and membrane thickness (Fig. 4(f-h)). We calculated η, η_2, and f_p at the actual resonant wavelength in the simulation, assuming it can be tuned to the target resonance later. The variation in the geometry will change the antenna resonant wavelength, but we can tune the resonant wavelength to the target value using e.g. gas tuning [30]. The antenna performance is robust to the bottom reflector distance as shown in Fig. 4(f). From Fig. 4(g) it is seen that increasing the hole size by 10% only decreases the efficiency by 2%, whereas a reduction in hole size by 10% reduces the efficiency by 12%. We observe a similar trend when decreasing rather than increasing the membrane thickness, as seen in Fig. 4(h). The spin-photon interface efficiency η does not decrease more than 12% for a ±10% geometry variation. The design with a large Purcell factor (Fig. 4(i)) maintains η_1 even though the Purcell factor decreases by 70% due to variations in dipole location, orientation, or nanostructure geometry. Within a ±10% geometry variation, η_2 does not decrease by more than 13% when the dipole is coupled to the antenna mode, which leads to a robust spin-photon interface efficiency η. Though our designs are resilient, remaining fabrication imperfection may affect the device performance. This can be overcome with parameter sweeps and tolerance optimized designs [30,31].

Finally, we study the size dependence of the antenna. We reduce the antenna size to $2L_x \times 2L_y$ where L_x and L_y are the length in the x and y direction. The simulation region is still 10 μm × 10 μm, where the diamond slab dimension is 10 μm $\times$ $2L_y$. The regions $y>L_y$ and $y<-L_y$ are filled by air as the undercut trench [32]. In Fig. 4(j), η will not reduce more than 5% when $L_x>2$ μm fixing $L_y = 5$ μm. When reducing L_y with the fixed $L_x = 5$ μm, we notice that η does not decrease more than 2% when $L_y>1.2$ μm. The η is over 73% with dimension 4 μm $\times$ 2.4 μm for an NV center which resonant wavelength is $\lambda = 637$ nm.

5. Conclusion

In conclusion, we introduced a transfer-matrix approach for cavity-grating designs, enabling efficient calculation of the cavity mode and the far field after an FDTD simulation of scattering matrix primitives. We applied this method to design an efficient dielectric antenna for quantum emitters. Specifically, the design achieves: (i) a relatively large emitter spacing to the first etched surface of 1.4 λ/n_{d} to alleviate surface charge noise; (ii) 93% mode overlap with a 0.4 NA Gaussian beam which has 99% collection efficiency within an NA of 0.5, together with a Purcell factor of 420; (iii) robustness to fabrication and dipole variations. While we considered a diamond membrane here, the design may apply to diverse materials such as Si or GaAs. We anticipate that our design methodology and the efficient quantum emitter interfaces benefit numerous applications, including multiplexed quantum repeaters [33], arrayed quantum sensors [18,34], boson sampling [35], and spin-based fault-tolerant quantum computers [9].

Funding. NSF QISE-NET Award (DMR-1747426); MITRE Quantum Moonshot Program; NSF STC Center for Integrated Quantum Materials (DMR-1231319); NSF EFRI ACQUIRE (EFMA-1641064); NSF Engineering Research Center for Quantum Networks (EEC-1941583); Air Force Office of Scientific Research (FA9550-14-1-0052); DARPA Driven and Nonequilibrium Quantum Systems (DRINQS) (HR001118S0024).

Acknowledgments. The authors thank Hamza Raniwala and Mohamed ElKabbash for useful comments. L. L. acknowledges support from the Analog Devices Fellowship. H. C. acknowledges the Claude E. Shannon Fellowship and Samsung Scholarship.

Disclosures. The authors declare no conflicts of interest.

Supplemental document. See Supplement 1 for supporting content.

References

1. M. W. Doherty, N. B. Manson, P. Delaney, F. Jelezko, J. Wrachtrup, and L. C. Hollenberg, "The nitrogen-vacancy colour centre in diamond," Phys. Rep. **528**(1), 1–45 (2013).
2. M. Leifgen, T. Schröder, F. Gädeke, R. Riemann, V. Métillon, E. Neu, C. Hepp, C. Arend, C. Becher, K. Lauritsen, and O. Benson, "Evaluation of nitrogen- and silicon-vacancy defect centres as single photon sources in quantum key distribution," New J. Phys. **16**(2), 023021 (2014).
3. T. Iwasaki, F. Ishibashi, Y. Miyamoto, Y. Doi, S. Kobayashi, T. Miyazaki, K. Tahara, K. D. Jahnke, L. J. Rogers, B. Naydenov, F. Jelezko, S. Yamasaki, S. Nagamachi, T. Inubushi, N. Mizuochi, and M. Hatano, "Germanium-Vacancy single color centers in diamond," Sci. Rep. **5**(1), 12882 (2015).
4. T. Iwasaki, Y. Miyamoto, T. Taniguchi, P. Siyushev, M. H. Metsch, F. Jelezko, and M. Hatano, "Tin-vacancy quantum emitters in diamond," Phys. Rev. Lett. **119**(25), 253601 (2017).
5. M. E. Trusheim, B. Pingault, N. H. Wan, M. Gündoğan, L. De Santis, R. Debroux, D. Gangloff, C. Purser, K. C. Chen, M. Walsh, J. J. Rose, J. N. Becker, B. Lienhard, E. Bersin, I. Paradeisanos, G. Wang, D. Lyzwa, A. R.-P. Montblanch, G. Malladi, H. Bakhru, A. C. Ferrari, I. A. Walmsley, M. Atatüre, and D. Englund, "Transform-Limited photons from a coherent Tin-Vacancy spin in diamond," Phys. Rev. Lett. **124**(2), 023602 (2020).
6. G. Thiering and A. Gali, "Ab initio Magneto-Optical spectrum of Group-IV vacancy color centers in diamond," Phys. Rev. X **8**(2), 021063 (2018).
7. M. Atatüre, D. Englund, N. Vamivakas, S.-Y. Lee, and J. Wrachtrup, "Material platforms for spin-based photonic quantum technologies," Nat. Rev. Mater. **3**(5), 38–51 (2018).
8. P. C. Humphreys, N. Kalb, J. P. J. Morits, R. N. Schouten, R. F. L. Vermeulen, D. J. Twitchen, M. Markham, and R. Hanson, "Deterministic delivery of remote entanglement on a quantum network," Nature **558**(7709), 268–273 (2018).
9. H. Choi, M. Pant, S. Guha, and D. Englund, "Percolation-based architecture for cluster state creation using photon-mediated entanglement between atomic memories," npj Quantum Inf. **5**(1), 104 (2019).
10. P. Cappellaro and A. Ajoy, "Stable three-axis nuclear spin gyroscope," (2016). US Patent 9, 417, 068.
11. N. H. Wan, B. J. Shields, D. Kim, S. Mouradian, B. Lienhard, M. Walsh, H. Bakhru, T. Schröder, and D. Englund, "Efficient extraction of light from a nitrogen-vacancy center in a diamond parabolic reflector," Nano Lett. **18**(5), 2787–2793 (2018).

Optics EXPRESS

12. J. Hadden, J. Harrison, A. Stanley-Clarke, L. Marseglia, Y.-L. Ho, B. Patton, J. O'Brien, and J. Rarity, "Strongly enhanced photon collection from diamond defect centers under microfabricated integrated solid immersion lenses," Appl. Phys. Lett. **97**(24), 241901 (2010).
13. O. J. Trojak, C. Woodhead, S.-I. Park, J. D. Song, R. J. Young, and L. Sapienza, "Combined metallic nano-rings and solid-immersion lenses for bright emission from single inas/gaas quantum dots," Appl. Phys. Lett. **112**(22), 221102 (2018).
14. J. Liu, R. Su, Y. Wei, B. Yao, S. F. C. da Silva, Y. Yu, J. Iles-Smith, K. Srinivasan, A. Rastelli, J. Li, and X. Wang, "A solid-state source of strongly entangled photon pairs with high brightness and indistinguishability," Nat. Nanotechnol. **14**(6), 586–593 (2019).
15. J. Zheng, A. C. Liapis, E. H. Chen, C. T. Black, and D. Englund, "Chirped circular dielectric gratings for near-unity collection efficiency from quantum emitters in bulk diamond," Opt. Express **25**(26), 32420–32435 (2017).
16. L. Li, E. H. Chen, J. Zheng, S. L. Mouradian, F. Dolde, T. Schröder, S. Karaveli, M. L. Markham, D. J. Twitchen, and D. Englund, "Efficient photon collection from a nitrogen vacancy center in a circular bullseye grating," Nano Lett. **15**(3), 1493–1497 (2015).
17. J. T. Choy, I. Bulu, B. J. Hausmann, E. Janitz, I.-C. Huang, and M. Lončar, "Spontaneous emission and collection efficiency enhancement of single emitters in diamond via plasmonic cavities and gratings," Appl. Phys. Lett. **103**(16), 161101 (2013).
18. L. Kim, H. Choi, M. Trusheim, and D. Englund, "Absorption-based diamond spin microscopy on a plasmonic quantum metasurface," arXiv preprint arXiv:2011.04885 (2020).
19. A. Karamlou, M. E. Trusheim, and D. Englund, "Metal-dielectric antennas for efficient photon collection from diamond color centers," Opt. Express **26**(3), 3341–3352 (2018).
20. S. I. Bogdanov, O. A. Makarova, X. Xu, Z. O. Martin, A. S. Lagutchev, M. Olinde, D. Shah, S. N. Chowdhury, A. R. Gabidullin, I. A. Ryzhikov, I. A. Rodionov, A. V. Kildishev, S. I. Bozhevolnyi, A. Boltasseva, V. M. Shalaev, and J. B. Khurgin, "Ultrafast quantum photonics enabled by coupling plasmonic nanocavities to strongly radiative antennas," Optica **7**(5), 463–469 (2020).
21. A. Arbabi, Y. Horie, M. Bagheri, and A. Faraon, "Dielectric metasurfaces for complete control of phase and polarization with subwavelength spatial resolution and high transmission," Nat. Nanotechnol. **10**(11), 937–943 (2015).
22. T.-Y. Huang, R. R. Grote, S. A. Mann, D. A. Hopper, A. L. Exarhos, G. G. Lopez, G. R. Kaighn, E. C. Garnett, and L. C. Bassett, "A monolithic immersion metalens for imaging solid-state quantum emitters," Nat. Commun. **10**(1), 1–8 (2019).
23. T. M. Babinec, B. M. Hausmann, M. Khan, Y. Zhang, J. Maze, P. R. Hemmer, and M. Lončar, "A bright single photon source based on a diamond nanowire," Nat. Nanotechnol. **5**(3), 195–199 (2010).
24. H. Choi, D. Zhu, Y. Yoon, and D. Englund, "Cascaded cavities boost the indistinguishability of imperfect quantum emitters," Phys. Rev. Lett. **122**(18), 183602 (2019).
25. A. Faraon, P. E. Barclay, C. Santori, K.-M. C. Fu, and R. G. Beausoleil, "Resonant enhancement of the zero-phonon emission from a colour centre in a diamond cavity," Nat. Photonics **5**(5), 301–305 (2011).
26. U. Levy and Y. Silberberg, "Weakly diverging to tightly focused gaussian beams: a single set of analytic expressions," J. Opt. Soc. Am. A **33**(10), 1999–2009 (2016).
27. M. Moharam, D. A. Pommet, E. B. Grann, and T. Gaylord, "Stable implementation of the rigorous coupled-wave analysis for surface-relief gratings: enhanced transmittance matrix approach," J. Opt. Soc. Am. A **12**(5), 1077–1086 (1995).
28. J. Lu, C. Petre, E. Yablonovitch, and J. Conway, "Numerical optimization of a grating coupler for the efficient excitation of surface plasmons at an ag-sio 2 interface," J. Opt. Soc. Am. B **24**(9), 2268–2272 (2007).
29. J. F. Ziegler, "Srim-2003," Nucl. Instrum. Methods Phys. Res., Sect. B **219-220**, 1027–1036 (2004).
30. L. Li, T. Schröder, E. H. Chen, M. Walsh, I. Bayn, J. Goldstein, O. Gaathon, M. E. Trusheim, M. Lu, J. Mower, M. Cotlet, M. L. Markham, D. J. Twitchen, and D. Englund, "Coherent spin control of a nanocavity-enhanced qubit in diamond," Nat. Commun. **6**(1), 6173 (2015).
31. A. Sipahigil, R. E. Evans, D. D. Sukachev, M. J. Burek, J. Borregaard, M. K. Bhaskar, C. T. Nguyen, J. L. Pacheco, H. A. Atikian, and C. Meuwly, "An integrated diamond nanophotonics platform for quantum-optical networks," Science **354**(6314), 847–850 (2016).
32. N. H. Wan, S. Mouradian, and D. Englund, "Two-dimensional photonic crystal slab nanocavities on bulk single-crystal diamond," Appl. Phys. Lett. **112**(14), 141102 (2018).
33. K. C. Chen, E. Bersin, and D. Englund, "A polarization encoded photon-to-spin interface," arXiv preprint arXiv:2004.02381 (2020).
34. A. M. Zagoskin, R. D. Wilson, M. Everitt, S. Savel'ev, D. R. Gulevich, J. Allen, V. Dubrovich, and E. Il'Ichev, "Spatially resolved single photon detection with a quantum sensor array," Sci. Rep. **3**(1), 3464 (2013).
35. H.-S. Zhong, H. Wang, Y.-H. Deng, M.-C. Chen, L.-C. Peng, Y.-H. Luo, J. Qin, D. Wu, X. Ding, Y. Hu, P. Hu, X.-Y. Yang, W.-J. Zhang, H. Li, Y. Li, X. Jiang, L. Gan, G. Yang, L. You, Z. Wang, L. Li, N.-L. Liu, C.-Y. Lu, and J.-W. Pan, "Quantum computational advantage using photons," Science **370**, 1460–1463 (2020).